Cross-sectional imaging of quenched region in a steel rod using energy-resolved neutron tomography

Watanabe, Kenichi
Nagoya University

Minniti, Triestino
STFC, Rutherford Appleton Laboratory, ISIS Facility

Sato, Hirotaka
Hokkaido University

Anton S. Tremsin
Space Science Laboratory, University of California at Berkeley

他

出版情報：Nuclear Instruments and Methods in Physics Research Section A: Accelerators, Spectrometers, Detectors and Associated Equipment. 944, pp.162532-, 2019-11-11. Elsevier
バージョン：
権利関係：

Cross-sectional imaging of quenched region in a steel rod using energy-resolved neutron tomography

Kenichi Watanabe[1], Triestino Minniti[2], Hirotaka Sato[3], Anton S. Tremsin[4], Winfried Kockelmann[2], Robert Dalgliesh[2], Yoshiaki Kiyanagi[1]

[1] Nagoya University, Furo-cho, Chikusa-ku, Nagoya, 464-8603, Japan

[2] STFC, Rutherford Appleton Laboratory, ISIS Facility, Harwell, OX11 0QX, United Kingdom

[3] Hokkaido University, Kita 8, Nishi 5, Kita-ku, Sapporo, Hokkaido, 060-0808, Japan

[4] Space Science Laboratory, University of California at Berkeley, CA 94720 Berkeley, U.S.A.

Email of corresponding author: k-watanabe@energy.nagoya-u.ac.jp

Abstract

We demonstrate the collection and analysis of energy-resolved neutron tomography for the nondestructive inspection of a martensite phase in a quenched iron rod. The energy-resolved (4D) tomography technique can extract the internal information of crystalline phase and microstructural features, such as the distribution of martensite. However, care must be taken when performing energy-resolved neutron tomography on a strongly textured sample in which the crystal grains are preferentially oriented and the neutron attenuation spectrum depends on the direction. As the standard tomography algorithm is based on the assumption that the attenuation is isotropic, anisotropy in the neutron attenuation distorts the reconstructed information. In other words, energy-resolved neutron tomography can be a powerful tool for nondestructive martensite observation in iron materials, which are usually not strongly textured.

KEYWORDS: *energy-resolved neutron imaging; neutron tomography; Bragg-edge analysis; quenched steel; martensite*

1. Introduction

In the last decade, various methods of energy-resolved neutron imaging have been developed as useful tools for materials science and engineering studies [1–5]. Among them, Bragg-edge transmission imaging using a pulsed neutron source has been recognized as a powerful analytical tool to nondestructively reveal the crystalline microstructural information in a bulk material with a spatial resolution of less than 1 mm over a large area. The material properties obtained by this technique are the crystal structure, crystalline phase, crystallographic texture, crystallite size, crystal lattice strain, and crystal microstrain, which are deduced by using the Rietveld-type Bragg-edge analysis code, Rietveld Imaging of Transmission Spectra (RITS) [6–8]. The Bragg-edge analysis has often been applied to the nondestructive imaging of residual strain and crystalline size in metal polycrystalline materials [7–13].

One of the useful applications of Bragg-edge imaging is the evaluation of spatial distribution of martensite in quenched ferritic steels [14]. The martensite is formed in carbon steels by rapid cooling or quenching of the austenite of iron, which allows for higher carbon content than the ferrite. In the quenching process, carbon atoms have no time to diffuse out of the crystal structure. Consequently, the face-centered cubic austenite transforms into a strained body-centered tetragonal martensite phase. The crystal lattice of martensite is distorted from the pure body-centered cubic structure. In the Bragg-edge analysis, as the wavelength of the edge represents the distance between lattice planes, the edge shape is considered to be broadened in the martensite. As evidence of the edge shape broadening in the martensite, Sato *et al.* confirmed the linear correlation between the Bragg-edge broadening and the Vickers hardness, which increases in the martensite, in quenched steel rods [14].

Since Bragg-edge imaging is performed in transmission, the information obtained with this technique is integrated or averaged along a neutron path at each position in a sample. This means that a simple Bragg-edge analysis extracts no information on depth distribution along the neutron path. Of course, the martensite phase is usually distributed near the surfaces of quenched samples. For example, quenched steel rods, which are widely used in various structures such as drive units in automobiles, have an outer-rim region of martensite. One of the applications of a martensite evaluation based on Bragg-edge analysis is a thickness

evaluation of the martensite phase in quenched steel rods. In order to obtain this information nondestructively, we have to irradiate the rod sample with neutrons from the side surface and apply the tomographic technique, although previous measurements were performed along a cylinder axis [14].

Some researchers combined the Bragg-edge analysis with the tomographic technique [15–17]. They all carried out the Bragg-edge analysis first, and then the tomography technique was applied using parameters extracted from the Bragg-edge analysis. Some of them performed three-dimensional mapping of crystallographic phase distribution [15]. Because the attenuation coefficient corresponding to each phase can be extracted from the Bragg-edge spectrum, the parameters obtained by the Bragg-edge analysis can directly be used for tomography. Others performed strain tomography [16-17]. This kind of problem requires any constraint condition or prerequisite to reconstruct an image. On the other hand, when the martensite phase is reconstructed from the Bragg-edge broadening by using a simple tomographic technique, the edge broadening should be proportional to the amount of the martensite phase. Although the edge broadening can be a good index of the martensite phase, there is no necessity of proportional relationship between the both. In this paper, we attempted real energy-resolved (4D) neutron tomography, which can reconstruct neutron attenuation spectra at all voxels in three-dimensional space. We can obtain a three-dimensional distribution of the Bragg-edge broadening, which is an index of the martensite phase, from the reconstructed neutron attenuation spectra. The tomographic technique can basically reconstruct a cross-sectional image for a sample with isotropic attenuation features. The quenched iron rods usually exhibit weak texture and isotropic Bragg-edge features [14]. Additionally, we discuss the applicability of an energy-resolved tomographic analysis for a strongly textured sample, in which the Bragg-edge shape or neutron attenuation has some variation in various directions.

2. Materials and methods

2.1. Neutron beamlines

The imaging experiments were conducted at the Larmor and IMAT beamlines at the ISIS pulsed

neutron source, UK. The Larmor is one of the beamlines of ISIS Target Station 2 (TS2), which operates at a 10-Hz repetition rate. This beamline is fundamentally a multipurpose instrument for small-angle neutron scattering (SANS), diffraction, and spectroscopy utilizing the Larmor precession of polarized neutrons. However, since the beam size of the Larmor is roughly 30 × 30 mm^2, it can also be used for imaging experiments. For this experiment, the neutron flight path length was 25.9 m. The neutron flux was roughly 5 × 10^6 $n/cm^2/s$.

The IMAT beamline is a neutron imaging and diffraction beamline at ISIS TS2 [18]. This beamline has a large beam size of 200 × 200 mm^2. The neutron flight path length was 56.4 m. Although the path length was quite long, the neutron flux was relatively high owing to the use of a neutron guide. The neutron flux in this experiment was 7 × 10^6 $n/cm^2/s$ for an L/D of 250. Since both beamlines viewed the same coupled liquid hydrogen moderator, they had similar neutron spectra.

2.2. Samples

We prepared two metal rod samples. **Figure 1** shows photographs of the samples. The first sample was a quenched steel rod. The ferritic iron rod was processed by induction hardening from a radial outer surface. The diameter and length of the rod were 26 mm and 20 mm, respectively. Only the outer region was considered to be a martensite phase. The second sample was a combined metal rod as an example of a textured sample. A copper cylinder was inserted into an iron hollow cylinder. The copper material is often textured [1]. The diameter and length of the rod were 24 mm and 25 mm, respectively. The energy-resolved neutron imaging of the quenched and combined metal rods was conducted using the Larmor and IMAT beamlines, respectively.

2.3. Neutron imaging detector

In order to acquire energy-resolved or time-resolved neutron images using the time-of-flight (TOF) method, we applied the neutron-sensitive microchannel plate (MCP)/Timepix2 detector [9,19]. The neutron-sensitive MCP used in this work contains boron in the glass matrix. Boron atoms work as a converter

from slow neutrons to energetic charged particles, which are reaction products in a $^{10}B(n, \alpha)^{7}Li$ reaction. When these energetic particles have an impact on the inner surfaces of MCP pores, which are hexagonally arranged with an approximately 10-μm pitch, several electrons are emitted and multiplied by the MCP. These multiplied electrons are read out with Timepix2 ASIC chips, which were developed at CERN [20]. The detector has 512 × 512 pixels with a 55-μm pixel size, and each pixel can be operated at the rate of 100 kHz/pixel. The entire sensitive area was 28 × 28 mm^2.

In the TOF experiments, the Timepix2 ASICs were operated in event timing mode, in which the time of arrival of individual neutron signals relative to the trigger signals was recorded. Each pixel in the Timepix2 has a 14-bit register, which is used to store the timing information. The stored data are periodically transferred to the data processing unit, which is based on field-programmable gate arrays (FPGA), at the end of every shutter period. The FPGA-based data processing unit creates three-dimensional histograms, with two dimensions in space and one dimension in neutron flight time. Since only one event can be stored in each pixel for a given shutter period, second or subsequent events are rejected until data are transferred at the end of the shutter period. This is called the overlap effect or counting loss effect. When irradiating the MCP/Timepix2 detector in a high neutron flux field, the TOF spectrum obtained with the event timing mode can be severely distorted owing to the overlap effect. Therefore, we applied a method to correct the overlap effect, which was proposed by Tremsin et al. [21, 22].

2.4. Image acquisition procedures

The rod sample was placed in front of the MCP/Timepix2 detector. The cylinder sample stood vertically on a rotation stage. The distance between the detector window and the sample center was roughly 35 mm. The rod sample was rotated on the rotation stage, and projection images were acquired. For the quenched rod, 75 projection images with a rotation step angle of 2.4° were acquired during 180° rotation at the Larmor beamline. Each projection image was separated into 1,205 slices with 20-μs steps in the TOF domain owing to the event timing mode in the MCP/Timepix2 detector. The recorded wavelength range was from 2 to 5 Å. Each projection was acquired for 40 min.

For the combined metal rod, 40 projection images with a rotation step angle of 4.6º were acquired during 180º rotation at the IMAT beamline. Each projection image was separated into 2,321 slices with 40-μs steps in the TOF domain. The recorded wavelength range was from 0 to 6.5 Å. Each projection was acquired for 30 min. For another check, we acquired images of both samples in the direction parallel to the cylinder axis.

3. Image reconstruction procedures

Figure 2 shows an example of image reconstruction procedures for the quenched rod measurements. In the measurements, each projection at a given angle is a time-resolved radiographic image and consists of a large number of TOF slices. First, since each pixel lacked a sufficient neutron count to determine the transmission, a pixel binning process was performed on all of the projection images. The number of binned pixels was determined depending on the statistics of the acquired data. The transmission images were then created by normalizing these projection images with the blank image that was acquired without any sample. Finally, the pixel size of the transmission images was 220×220 μm^2. Neutron counts in a specific TOF bin correspond to the number of monoenergetic or given wavelength neutrons. By picking up the TOF slices in a specific TOF bin, we obtained monoenergetic neutron projection images for tomography.

A sinogram was then generated by collecting horizontal line profiles at a given vertical position from these projection images. A cross-sectional image can be reconstructed from the sinogram by the maximum-likelihood expectation-maximization (ML-EM) algorithm, which is an iterative tomography reconstruction algorithm [23]. A three-dimensional attenuation coefficient dataset was created by stacking these cross-sectional images. By repeating the same procedures for all TOF bins, we obtained the four-dimensional (3D in space and 1D in TOF or wavelength) attenuation coefficient data. By picking up slice images in a given plane from the tomographic images of all TOF bins, a time-resolved or energy-resolved cross-sectional slice of the neutron attenuation coefficient was obtained. The wavelength dependency of the neutron attenuation, such as the Bragg edge, can be created by arranging the image pixel

values in order of the TOF or wavelength.

4. Results and discussion

4.1. Quenched iron rod

First, a radiographic transmission image of the quenched rod in the direction parallel to the rod axis is shown in **Fig. 3 a)** for comparison purposes. The wavelength dependencies of the attenuation averaged in the square regions in Fig. 3 a) are shown in **Fig. 3 b)**. The attenuation A is derived by the following equation:

$$A = -\ln T \quad (1),$$

where A and T are the attenuation and transmission, respectively. The largest edge at 4 Å corresponds to the (110) plane of ferrite. In this edge, we can see a clear difference in the edge shape between the rim and the center region, with the rim region exhibiting a broader edge than the center. This is because the martensite phase, in which the edge width is broader than that in the ferrite phase, was formed in the rim region by the quenching process, as mentioned in the Introduction section [14]. In addition, the edge top shape in the center region is slightly sharper than that in the rim region. This indicates that crystal grains in the center region are preferentially oriented relative to the neutron beam direction. On the other hand, the grains in the rim region are assumed to be more randomly oriented in the martensite phase.

Figure 4 shows a radiographic transmission image of the quenched rod in the direction perpendicular to the rod axis. For a spectrum shape comparison, the rim region spectrum normalized with the center region is also plotted. For the nondestructive testing of a long steel rod, the inspection should be conducted based on measurements from this direction. Although the outer-rim region consists of the martensitic phase, differences in the (110) edge shapes between the center and rim regions are quite small. This is because both the core and the rim of the rod are superimposed in the central region of the radiograph from this direction. Since it is difficult to inspect the martensite in a steel rod by simple radiography from this direction, tomography is required.

Figure 5 shows a vertical center slice of the quenched rod obtained from the tomography

measurements and the wavelength dependencies of the attenuation averaged in the square regions of interest in **Fig. 5 a)**. A clear difference in the (110) Bragg-edge shapes between the ferrite and martensite phases can be seen in **Fig. 5 b)**. Since the tomographic technique extracts the internal information without superposition of the surface information, different features between the center and rim regions can be clearly seen. In addition, the (110) edge top in the center region has a round shape. This is in contrast to the case of Fig. 3 b), in which the radiography was acquired in the direction parallel to the rod axis. This is clear evidence that the edge shapes might have some differences in images acquired from different directions owing to the preferred orientation of the crystal grains.

To clearly extract some crystallographic features, we fitted the attenuation spectrum data to the edge function by using modified RITS code in the single-edge profile analysis mode [14]. In this fitting code, the Jorgensen profile function common in the TOF diffraction was used. In this function, the diffraction peak profile consists of exponential rise and exponential decay components and is convoluted with the Gaussian function. Although the original Jorgensen function has a single exponential decay component, in this paper, we applied the function with double exponential decay components for the spectrum used in these experiments. The edge function was consequently derived by integrating the diffraction peak function and is given as follows:

$$R(t) = (1-r)R_1(t) + rR_2(t) \quad (2),$$

where

$$R_i(t) = \frac{erfc(w)}{2} - \frac{\beta_i \exp(u)erfc(y) - \alpha \exp(v_i)erfc(z_i)}{2(\alpha+\beta_i)}, i = 1, 2 \quad (3).$$

$$\left(\begin{array}{l} t = \lambda - 2d,\ u = \frac{\alpha}{2}\left(\alpha\sigma^2 + 2t\right),\ v_i = \frac{\beta_i}{2}\left(\beta_i\sigma^2 - 2t\right) \\ w = \frac{t}{\sqrt{2}\sigma},\ y = \frac{\left(\alpha\sigma^2 + t\right)}{\sqrt{2}\sigma},\ z_i = \frac{\left(\beta_i\sigma^2 - t\right)}{\sqrt{2}\sigma} \end{array} \right)$$

where α and β_i are the exponential rise and decay constants of the diffraction peak function, respectively. In addition, r: fraction of the second decay component, σ: standard deviation of the Gaussian function, λ: neutron wavelength, and d: d-spacing of the crystal lattice. **Figure 6** shows two-dimensional maps of the extracted parameters from the Bragg-edge spectra at each pixel in the cross-sectional slice obtained by steel

rod tomography. The extracted parameters are the edge position and broadening of the (110) edge. The edge position and broadening corresponds to $2d$ and σ in Eq. (3), respectively. In particular, the edge-broadening map has a clear contrast between the center and rim regions. The rim region has a broader edge and shows typical features of the martensite phase. For a comparison purpose, **Figure 7** shows two-dimensional maps of the extracted Bragg-edge parameters obtained from the radiographic transmission image in the direction parallel to the rod axis shown in Fig. 3. It can be confirmed that the extracted Bragg-edge parameters from the tomographic image agreed with that from the radiographic image in the direction parallel to the rod axis. In addition, we confirmed the thickness of the martensite phase by measuring the Vickers hardness. The thickness of a higher hardness region was roughly 5 mm from the outer surface. This is also consistent with the results obtained from the tomography. The tomography technique allows for nondestructive inspection of the martensite thickness in a long rod sample.

4.2. Combined metal rod of iron and textured copper

As a second example for energy-resolved neutron tomography, we measured the combined metal rod. **Figure 8** shows a radiographic transmission image of the test object in the direction parallel to the rod axis. The rim region of iron has typical ferrite Bragg edges that correspond to a body-centered cubic (bcc) structure. On the other hand, the center region of copper has a face-centered cubic (fcc)-like structure. Although the edge positions of the (111) and (200) planes of copper were reproduced, the entire Bragg-edge shape was severely distorted. Although we can clearly see different phases between the ferrite and the copper, we have to note that the copper crystal grains are strongly textured or oriented in a preferential direction.

Figure 9 shows a horizontal slice of the combined metal rod as reconstructed from the tomography measurements and the wavelength dependencies of the attenuation averaged in the square regions in **Fig. 9 a)**. A clear difference in the Bragg-edge shape between the ferrite and the copper phases can be seen. However, in particular, the center region of the copper is distorted from the simple fcc structure and seems to be influenced by the rim region, which has a ferrite bcc structure. This is because neutron attenuation in a sample

with preferred oriented crystal grains depends on the direction of the projection. Since a normal tomography technique is based on the assumption that the attenuation is isotropic, anisotropy in the neutron attenuation distorts the reconstructed information. Therefore, we have to pay close attention when performing energy-resolved neutron tomography on a sample with strongly oriented crystal grains or a strongly textured sample. Conversely, we conclude that the tomography technique is useful for the nondestructive martensite observation of iron materials, which are usually not strongly textured.

5. Conclusions

We demonstrated energy-resolved (4D) neutron tomography for the nondestructive inspection of a martensite phase in a quenched iron rod. We confirmed that the tomography technique is useful in extracting the internal information of crystalline microstructural features such as the martensite phase distribution. We attempted to apply this technique to a strongly textured sample. Note that close attention should be paid when performing energy-resolved neutron tomography for a sample with strongly oriented crystal grains, such as a textured sample. Since the tomography technique is based on the assumption that the attenuation is isotropic, anisotropy in the neutron attenuation distorts the reconstructed information. Conversely, we conclude that the tomography technique is useful for nondestructive martensite observation in iron materials, which are usually not strongly textured.

Acknowledgements

This work was partially supported by the JSPS Program for Advancing Strategic International Networks to Accelerate the Circulation of Talented Researchers. We would like to thank Editage for English language editing.

References

[1] W. Kockelmann, G. Frei, E.H. Lehmann, P. Vontobel, J.R. Santisteban, Energy-selective neutron transmission imaging at a pulsed source., *Nucl. Instrum. Methods Phys. Res. Sec. A*, **578**, 421–434 (2007).

[2] T. Shinohara, T. Kai, K. Oikawa, M. Segawa, M. Harada, T. Nakatani, M. Ooi, K. Aizawa, H. Sato, T. Kamiyama, H. Yokota, T. Sera, K. Mochiki, Y. Kiyanagi, Final design of the energy-resolved neutron imaging system RADEN at J-PARC., *J. Phys. Conf. Ser.*, **746**, 746, 012007 (2016).

[3] M. Strobl, Future prospects of imaging at spallation neutron sources. *Nucl. Instrum. Methods Phys. Res. Sec. A*, **604**, 646–652 (2009).

[4] M. Strobl, N. Kardjilov, A. Hilger, D. Penumadu, I. Manke, Advanced neutron imaging methods with a potential to benefit from pulsed sources., *Nucl. Instrum. Methods Phys. Res. Sec. A*, **651**, 57–61 (2011).

[5] E. H. Lehmann, S. Peetermans, L. Josic, H. Leber, H. van Swygenhoven, Energy-selective neutron imaging with high spatial resolution and its impact on the study of crystalline-structured materials, *Nucl. Instrum. Methods Phys. Res. Sec. A*, **735**, 102–109 (2014).

[6] H. Sato, T. Kamiyama, Y. Kiyanagi, A Rietveld-type analysis code for pulsed neutron bragg-edge transmission imaging and quantitative evaluation of texture and microstructure of a welded α-iron plate, *Materials Transactions*, **52**, 1294–1302 (2011).

[7] H. Sato, T. Shinohara, R. Kiyanagi, K. Aizawa, M. Ooi, M. Harada, K. Oikawa, F. Maekawa, K. Iwase, T. Kamiyama Y. Kiyanagi, Upgrade of Bragg edge analysis techniques of the RITS code for crystalline structural information imaging, *Physics Procedia*, **43**, 186–195 (2013).

[8] H. Sato, K. Watanabe, K. Kiyokawa, R. Kiyanagi, K. Y. Hara, T. Kamiyama, M. Furusaka, T. Shinohara, Y. Kiyanagi, Further improvement of the RITS code for pulsed neutron bragg-edge transmission imaging, *Physics Procedia*, **88**, 322–330 (2017).

[9] A.S. Tremsin, J.B. McPhate, J.V. Vallerga, O.H.W. Siegmund, W. Kockelmann, A. Steuwer,

W.B. Feller, " High-resolution neutron counting sensor in strain mapping through transmission bragg edge diffraction," *IEEE Sensors Journal*, **11,** 3433–3436 (2011).

[10] Y. Su, K. Oikawa, S. Harjo, T. Shinohara, T. Kai, M. Harada, K. Hiroi, S. Zhang, J. D. Parker, H. Sato, Y. Shiota, Y. Kiyanagi and Y. Tomota, Time-of-flight neutron Bragg-edge transmission imaging of microstructures in bent steel plates, *Materials Science and Engineering A*, 675, 19–31 (2016).

[11] K. Oikawa, Y. H. Su, Y. Tomota, T. Kawasaki, T. Shinohara, T. Kai, K. Hiroi, S. Y. Zhang, J. D. Parker, H. Sato and Y. Kiyanagi, A comparative study of the crystallite size and the dislocation density of bent steel plates using Bragg-edge transmission imaging, TOF neutron diffraction and EBSD, *Physics Procedia*, 88, 34–41 (2017).

[12] Y. Shiota, H. Hasemi, Y. Kiyanagi, Crystallographic analysis of a Japanese sword by using Bragg edge transmission spectroscopy, *Physics Procedia*, **88**, 128–133 (2017).

[13] K. Oikawa, Y. H. Su, R. Kiyanagi, T. Kawasaki, T. Shinohara, T. Kai, K. Hiroi, S. Harjo, J. D. Parker, Y. Matsumoto, H. Hayashida, S. Y. Zhang, Y. Tomota and H. Sato, Recent progress on practical materials study by Bragg edge imaging at J-PARC, *Physica B: Condensed Matter*, **551**, 436–442 (2018).

[14] H. Sato, T. Sato, Y. Shiota, T. Kamiyama, A. S. Tremsin, M. Ohnuma, Y. Kiyanagi, Relation between Vickers hardness and Bragg-edge broadening in quenched steel rods observed by pulsed neutron transmission imaging, *Materials Transactions*, **56**, 1147–1152 (2015).

[15] Robin Woracek, Dayakar Penumadu, Nikolay Kardjilov, Andre Hilger, Mirko Boin, John Banhart, Ingo Manke, Neutron Bragg edge tomography for phase mapping, *Physics Procedia*, **69**, 227-236 (2015).

[16] H. Sato, Y. Shiota, T. Shinohara, T. Kamiyama, M. Ohnuma, M. Furusaka, Y. Kiyanagi, Development of the tensor CT algorithm for strain tomography using Bragg-edge neutron transmission, *Phys. Procedia*, **69**, 349–357 (2015).

[17] J.N. Hendriks, A.W.T. Gregg, C.M. Wensrich, A.S. Tremsin, T. Shinohara, M. Meylan, E.H.

Kisi, V. Luzin, O. Kirsten, Bragg-edge elastic strain tomography for in situ systems from energy-resolved neutron transmission imaging, *Phys. Rev. Materials*, **1**, 053802 (2017).

[18] T. Minniti, K. Watanabe, G. Burca, D. E. Pooley, W. Kockelmann, Characterization of the new neutron imaging and materials science facility IMAT, *Nucl. Instrum. Methods Phys. Res. Sec. A*, **888**, 184–195 (2018).

[19] A.S. Tremsin, J.B. McPhate, J.V. Vallerga, O.H.W. Siegmund, J.S. Hull, W.B. Feller, E. Lehmann, High-resolution neutron radiography with microchannel plates: Proof-of-principle experiments at PSI, *Nucl. Instrum. Methods Phys. Res. Sec. A*, **605**, 103–106 (2009).

[20] X. Llopart, R. Ballabriga, M. Campbell, L. Tlustos, W. Wong, Timepix, a 65k programmable pixel readout chip for arrival time, energy and/or photon counting measurements, *Nucl. Instrum. Methods Phys. Res. Sec. A*, **581**, 485–494 (2007).

[21] A.S. Tremsin, J.V. Vallerga, J.B. McPhate, O.H.W. Siegmund, Optimization of Timepix count rate capabilities for the applications with a periodic input signal, *Journal of Instrumentation*, **9**, C05026 (2014).

[22] K. Watanabe, T. Minniti, W. Kockelmann, R. Dalgliesh, G. Burca, A. S. Tremsin, Characterization of a neutron sensitive MCP/Timepix detector for quantitative image analysis at a pulsed neutron source, *Nucl. Instrum. Methods Phys. Res. Sec. A*, **861**, 55–63 (2017).

[23] K. Lange, R. Carson, EM reconstruction algorithms for emission and transmission tomography, *J. Comput. Assist. Tomogr.* **8**, 306–316 (1984).

Figure Captions

Figure 1 Photographs of metal rod samples. a) Quenched steel rod. Diameter 26 mm × length 20 mm. b) Combined metal rod. Outer region: iron with diameter 24 mm × length 25 mm; inner region: copper with diameter 10 mm × length 25 mm.

Figure 2 Image reconstruction procedures for example of quenched rod measurements.

Figure 3 a) Radiographic transmission image of quenched rod obtained in direction parallel to rod axis at the wavelength of 4.095 angstrom and b) neutron attenuation spectra averaged in square regions in Fig. 3 a).

Figure 4 a) Radiographic transmission image of quenched rod obtained in direction perpendicular to rod axis at the wavelength of 4.095 angstrom and b) neutron attenuation spectra averaged in square regions in Fig. 4 a). For spectrum shape comparison, rim region spectrum multiplied by 2.2 is also plotted.

Figure 5 a) Vertical slice reconstructed by quenched rod tomography at the wavelength of 4.062 angstrom and b) neutron attenuation spectra averaged in square regions in Fig. 5 a).

Figure 6 Map of a) edge position and b) broadening of (110) edge extracted from energy-resolved tomographic slice. c) Line profile of edge broadening in Fig. 6 b).

Figure 7 Map of a) edge position and b) broadening of (110) edge extracted from radiographic transmission image obtained in direction parallel to rod axis. c) Line profile of edge broadening in Fig. 7 b).

Figure 8 a) Radiographic transmission image of combined metal rod obtained in direction perpendicular to rod axis at the wavelength of 4.150 angstrom and b) neutron attenuation spectra averaged in square regions in Fig. 7 a).

Figure 9 a) Horizontal slice reconstructed by combined metal rod tomography at the wavelength of 4.137 angstrom and b) neutron attenuation spectra averaged in square regions in Fig. 8 a).

a)

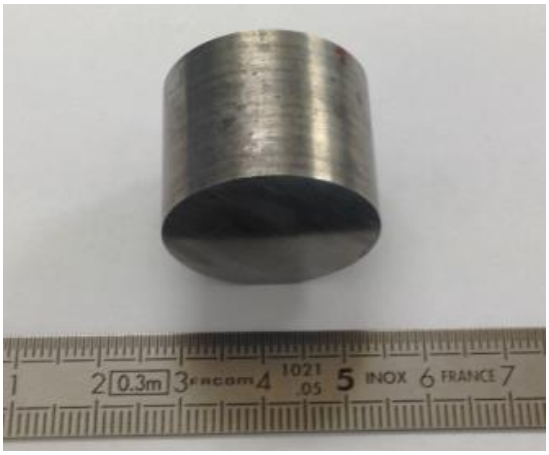

b)

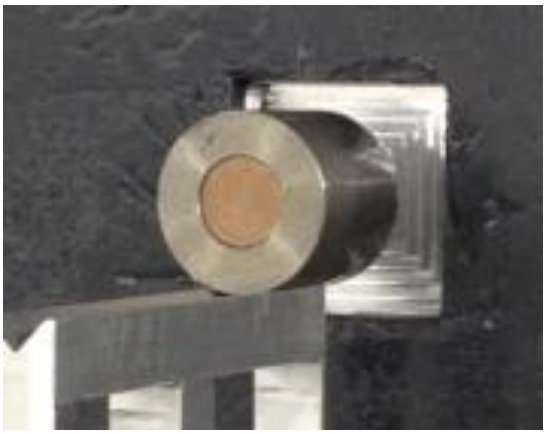

Figure 1 Photographs of metal rod samples. a) Quenched steel rod. Diameter 26 mm × length 20 mm. b) Combined metal rod. Outer region: iron with diameter 24 mm × length 25 mm; inner region: copper with diameter 10 mm × length 25 mm.

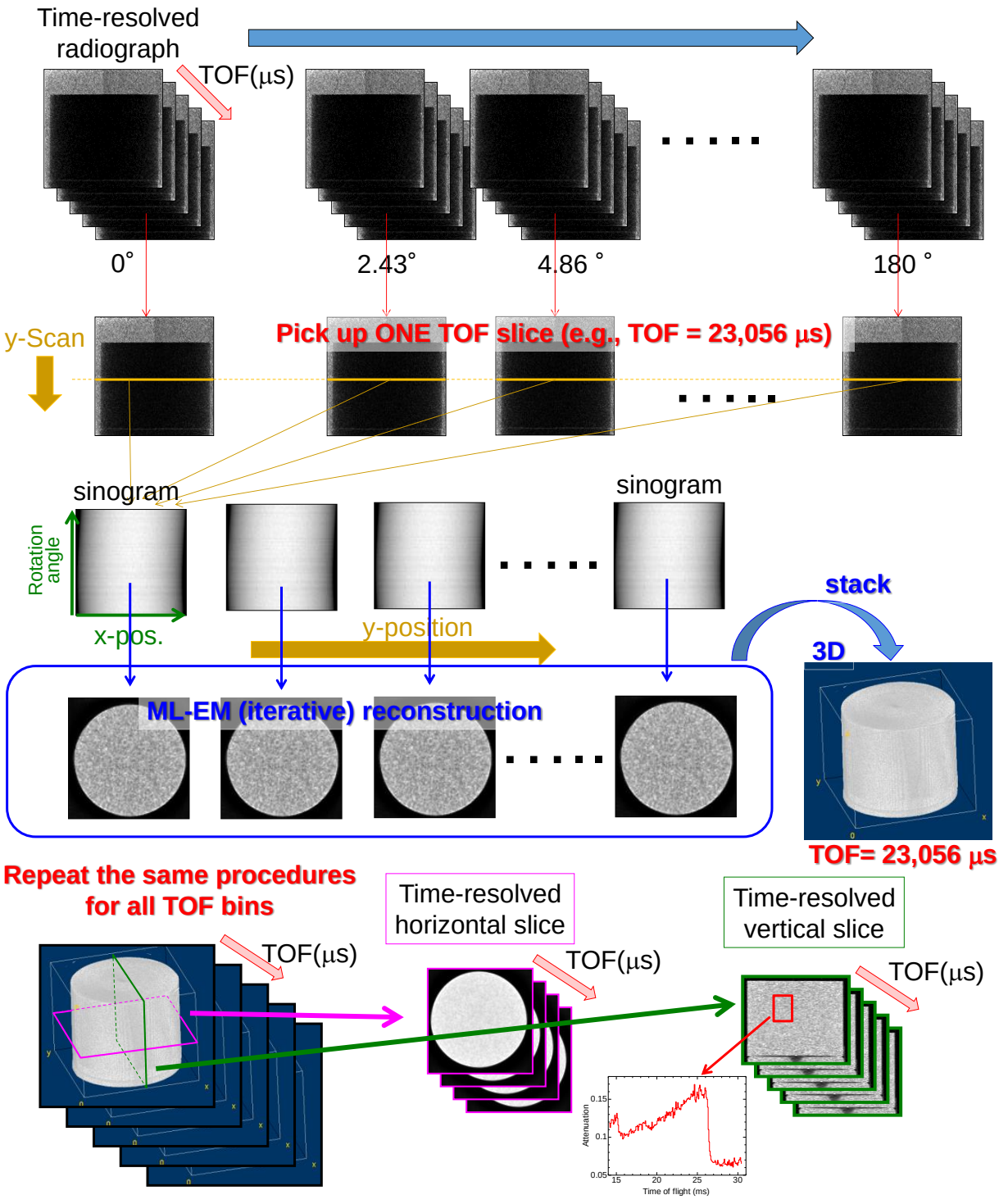

Figure 2 Image reconstruction procedures for example of quenched rod measurements.

a)

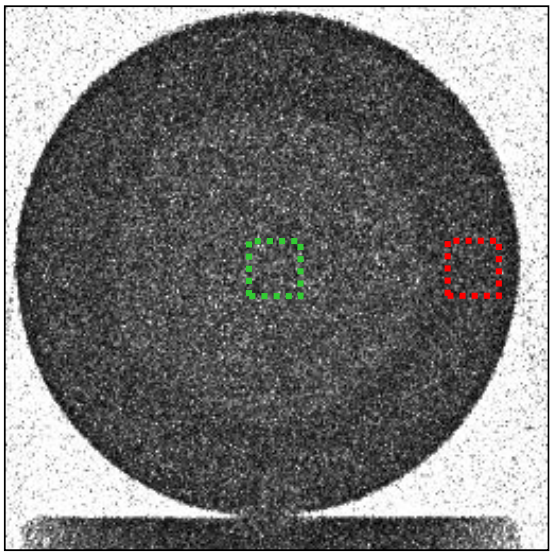

b)

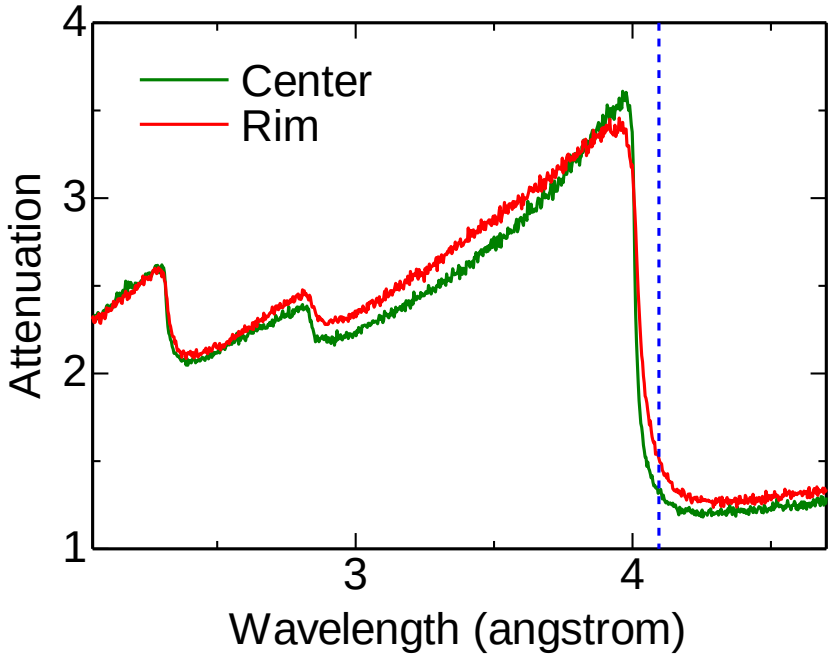

Figure 3 a) Radiographic transmission image of quenched rod obtained in direction parallel to rod axis at the wavelength of 4.095 angstrom and b) neutron attenuation spectra averaged in square regions in Fig. 3 a).

a)

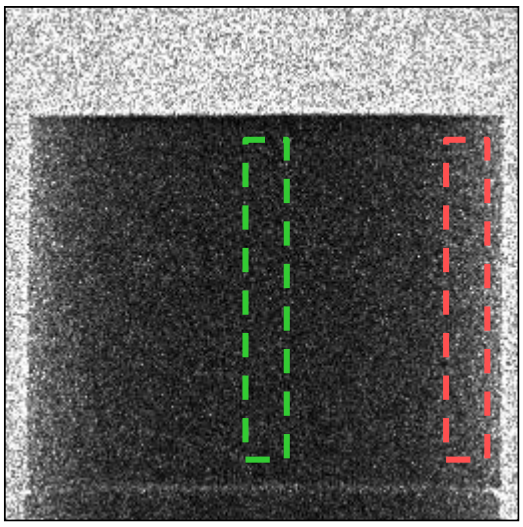

b)

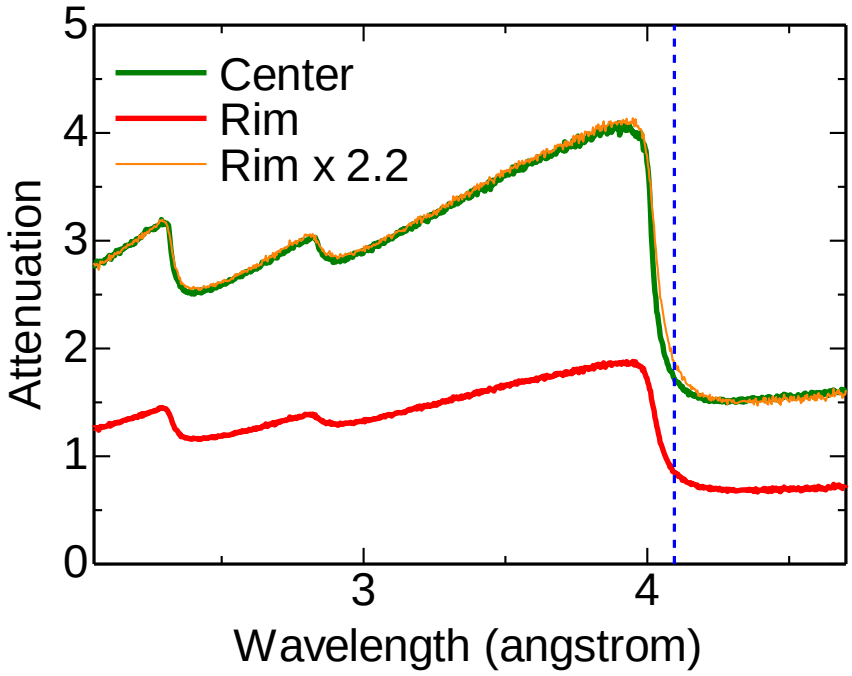

Figure 4 a) Radiographic transmission image of quenched rod obtained in direction perpendicular to rod axis at the wavelength of 4.095 angstrom and b) neutron attenuation spectra averaged in square regions in Fig. 4 a). For spectrum shape comparison, rim region spectrum multiplied by 2.2 is also plotted.

a)

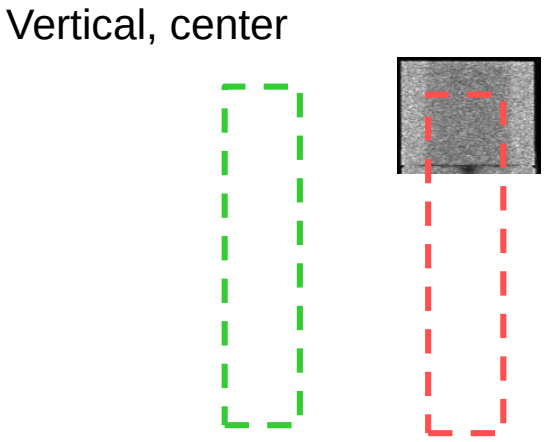

b)

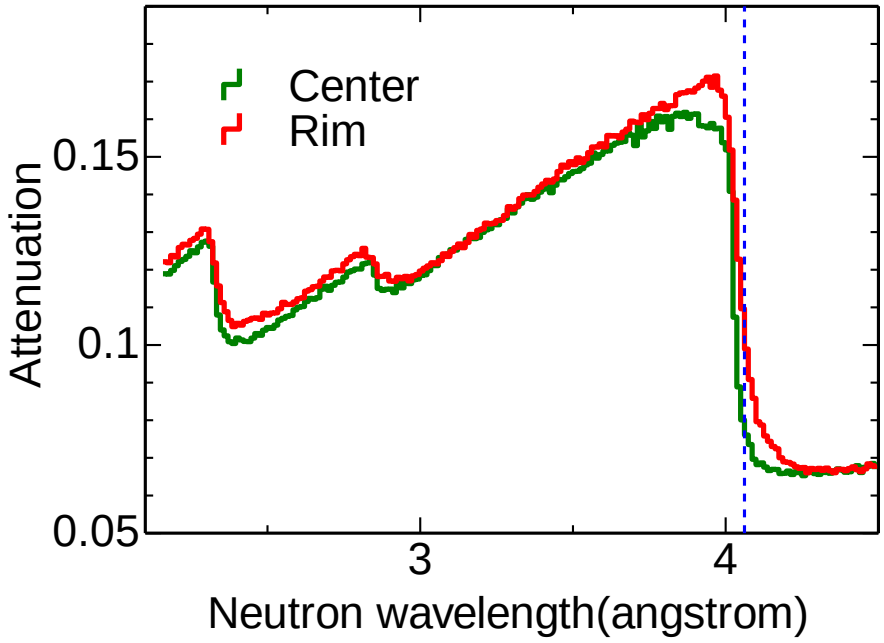

Figure 5 a) Vertical slice reconstructed by quenched rod tomography at the wavelength of 4.062 angstrom and b) neutron attenuation spectra averaged in square regions in Fig. 5 a).

a) b)

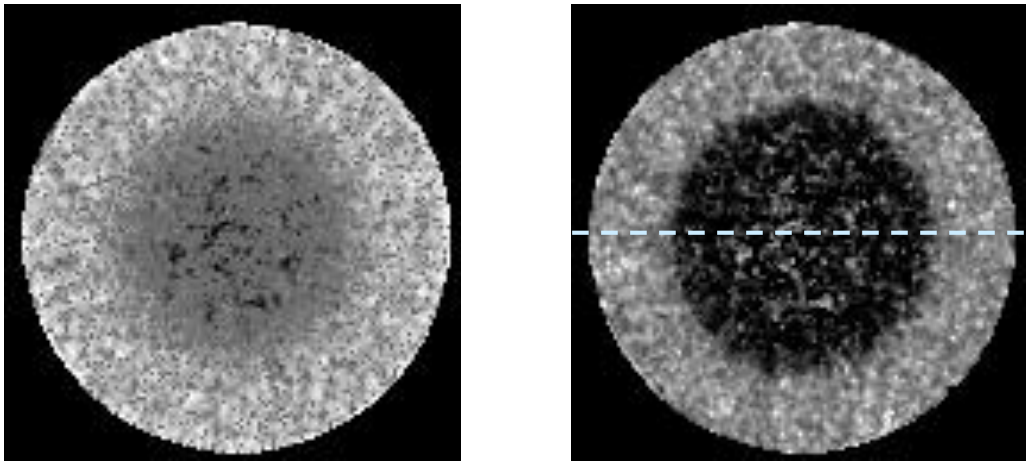

c)

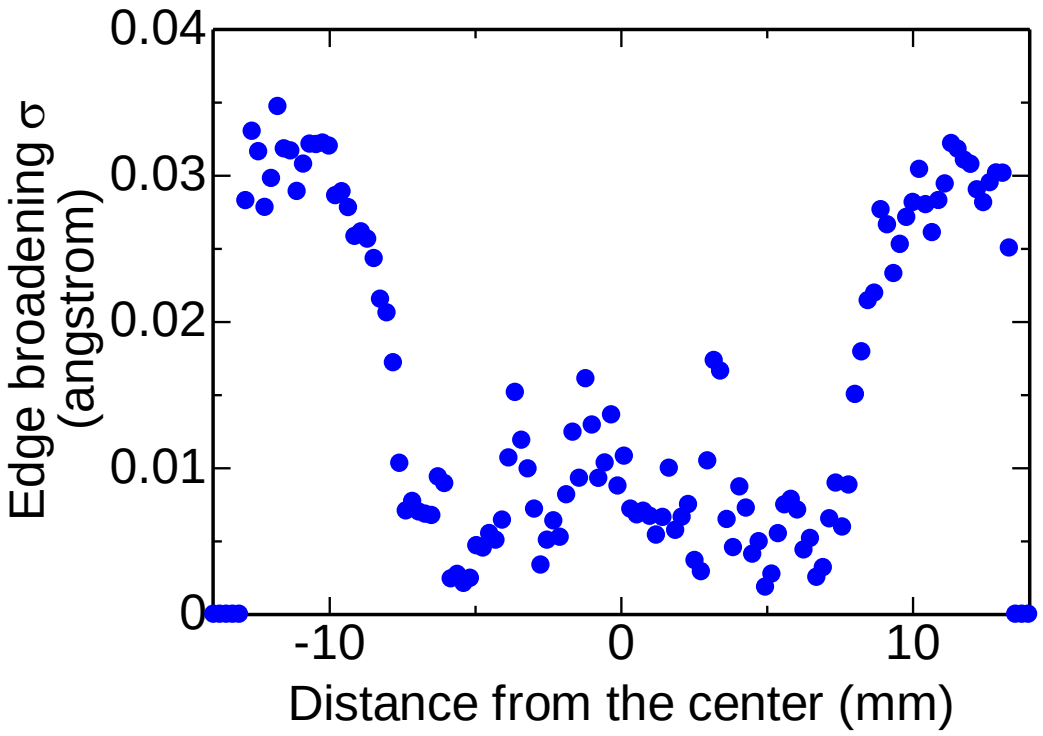

Figure 6 Map of a) edge position and b) broadening of (110) edge extracted from energy-resolved tomographic slice. c) Line profile of edge broadening in Fig. 6 b).

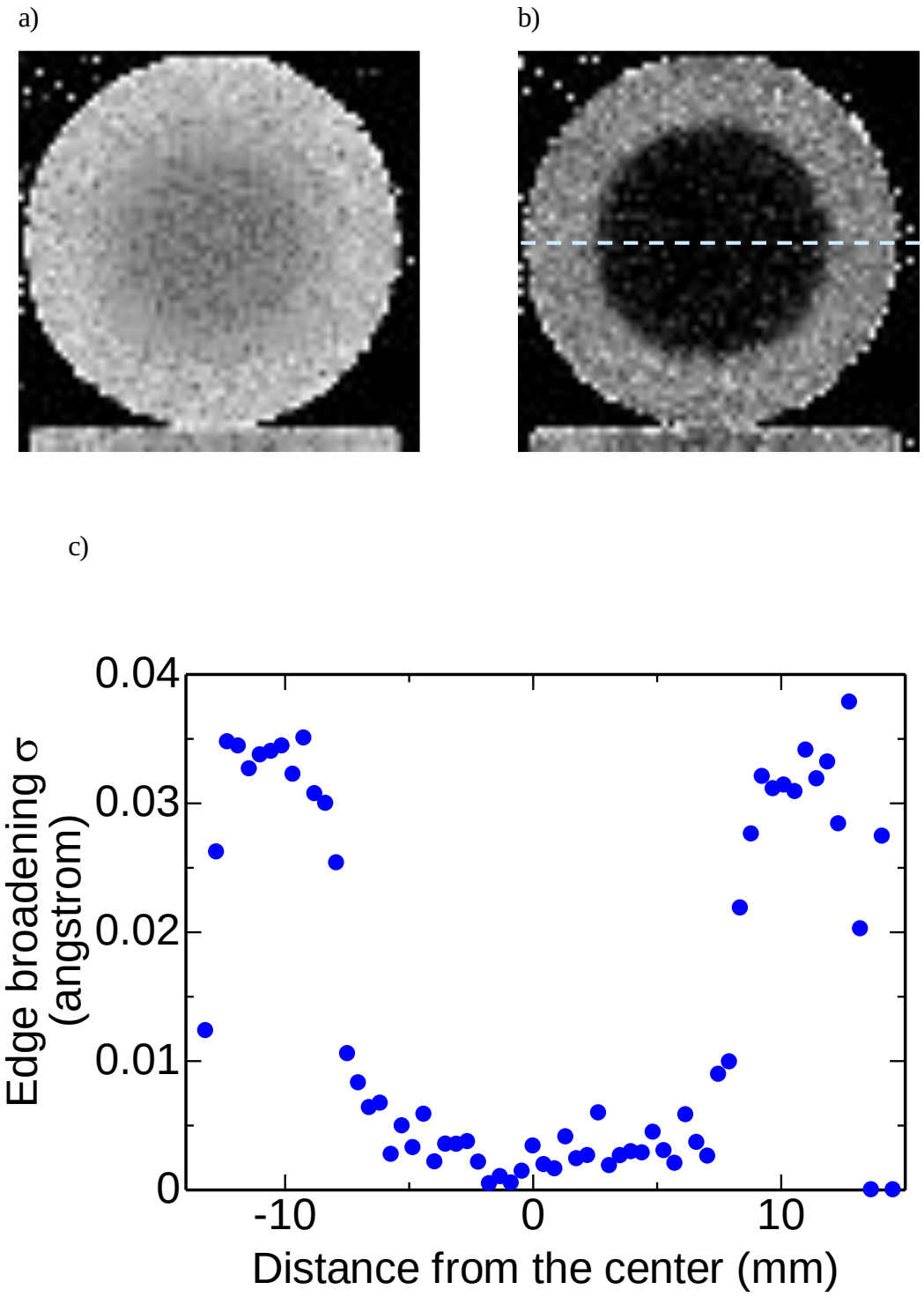

Figure 7 Map of a) edge position and b) broadening of (110) edge extracted from radiographic transmission image obtained in direction parallel to rod axis. c) Line profile of edge broadening in Fig. 7 b).

a)

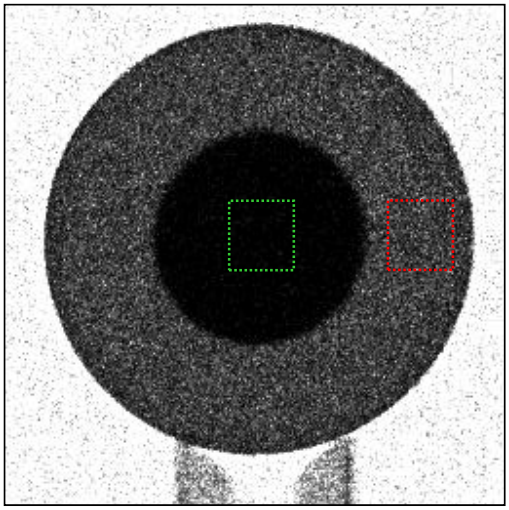

b)

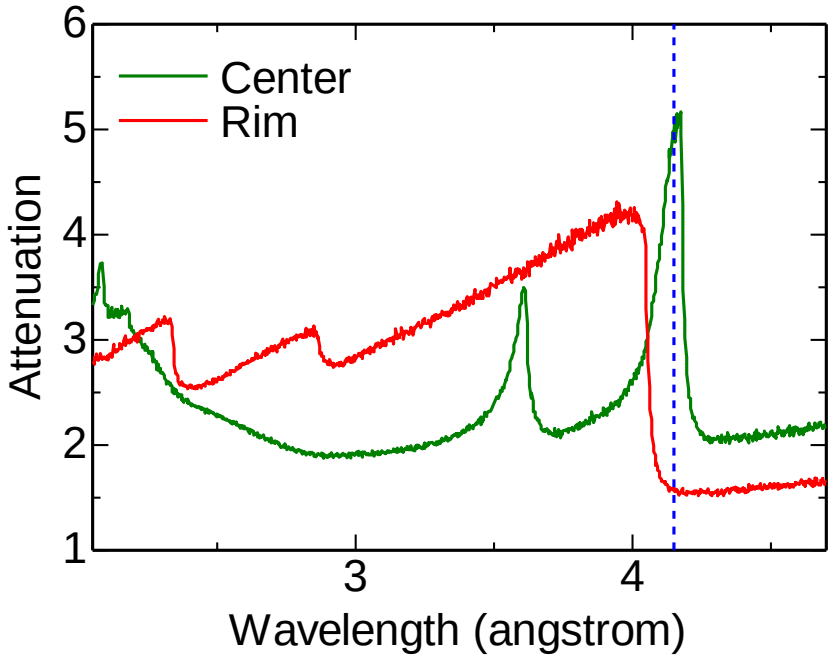

Figure 8 a) Radiographic transmission image of combined metal rod obtained in direction perpendicular to rod axis at the wavelength of 4.150 angstrom and b) neutron attenuation spectra averaged in square regions in Fig. 7 a).

a)

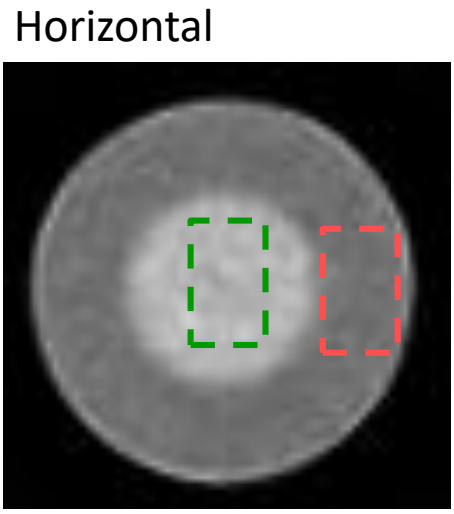

b)

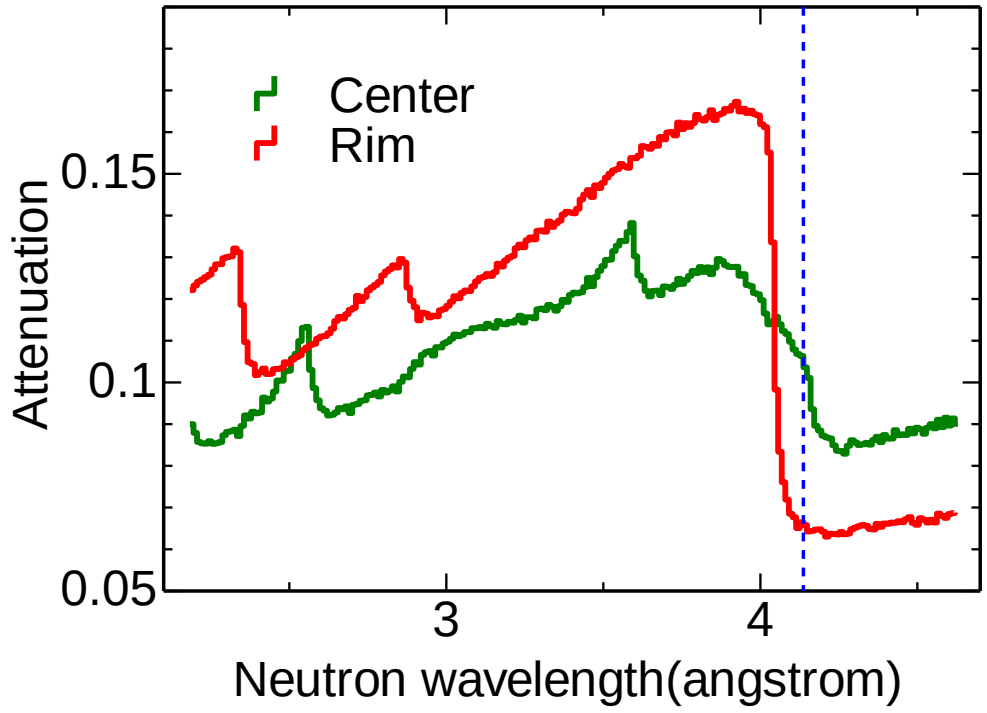

Figure 9 a) Horizontal slice reconstructed by combined metal rod tomography at the wavelength of 4.137 angstrom and b) neutron attenuation spectra averaged in square regions in Fig. 8 a).